Modeled F Region Response to Auroral Dynamics Based Upon Dynamics Explorer Auroral Observations

J. J. Sojka and R. W. Schunk

Center for Atmospheric and Space Sciences, Utah State University, Logan

J. D. Craven and L. A. Frank

Department of Physics and Astronomy, University of Iowa, Iowa City

J. Sharber and J. D. Winningham

Southwest Research Institute, San Antonio, Texas

Auroral images from the Dynamics Explorer 1 (DE 1) scanning auroral imager have been combined with in situ auroral precipitation data from the DE 2 low altitude plasma instrument to form a time-dependent global auroral energy flux model. This model has both good time (12 min) and spatial (100 km) resolution compared to that currently available for global scale ionospheric and thermospheric modeling. The development and comparison of this model with others are discussed. Data from an aurorally active period, November 25, 1981, are presented and used as a case study for this model. Using a global ionospheric model, the effect of the DE auroral model is contrasted with that of a conventional empirical auroral energy flux model. Major differences in the modeled F region ionosphere are predicted from this comparative study. Specifically, F region densities differ by factors of two to four, while density boundary locations differ by up to 5° in latitude. The results indicate that "pixel size" auroral fine-structure must be included in the global ionosphere and thermosphere models when they are tested against specific ground-based or satellite data sets if an unambiguous result is to be obtained. The longer time constants of the F region are not enough to smooth-out the auroral (spatial and temporal) dynamics.

1. Introduction

Theoretical models of the terrestrial ionosphere and thermosphere have now attained global-scale [*Sojka and Schunk*, 1985; *Roble et al.*, 1987; *Fuller-Rowell et al.*, 1987]. Such models require global-scale inputs, specifically for the magnetospheric contribution. At the present time no global-scale theoretical model of the magnetosphere exists. Hence, statistical (empirical) models of the magnetospheric electric field [*Volland*, 1978; *Heelis et al.*, 1982; *Sojka et al.*, 1986; *Heppner and Maynard*, 1987] and the auroral precipitation [*Spiro et al.*, 1982; *Hardy et al.*, 1985; *Evans*, 1987] are used as inputs to ionospheric and thermospheric models. Such studies are handicapped because statistical inputs cannot readily be made to simulate the spatial variations and temporal dynamics of geomagnetic storms and substorms. To minimize some of these difficulties, models have used in-situ satellite observations of auroral precipitation and electric fields combined with Defense Meteorological Satellite Program (DMSP) images and ground-based incoherent scatter radar observations of electric fields to define the auroral and convection boundaries [*Sojka et al.*, 1983; *Rasmussen et al.*, 1986]. With the availability of global auroral image sequences from the Dynamics Explorer 1 (DE 1) satellite, it is possible to directly define a magnetospheric auroral input on the scale needed by the ionospheric and thermospheric models. To this end, we have performed an investigation

in which model ionospheric responses obtained with DE 1 auroral images providing the auroral input are contrasted with the conventional empirical method of defining the auroral input.

Auroral observations have advanced significantly in the last few years through the increased use of ground-based photometers and all-sky cameras, and low-altitude satellites (e.g., the polar-orbiting DMSP and National Oceanic and Atmospheric Administration (NOAA) satellites) make regular in-situ measurements of auroral precipitation; the DMSP satellites provide a large data base of auroral images along their satellite tracks. With the launch of the high-altitude Dynamics Explorer 1 satellite, the first time-sequences of auroral images have become available to yield information on auroral dynamics on a global scale with a spatial resolution of $\lesssim 100$ km and a temporal resolution of 12 min or better. Such scale lengths and sampling rates are in line with the requirements of global ionosphere and thermosphere models. The auroral images are complemented by in-situ measurements of auroral precipitation by the low altitude plasma instrument (LAPI) on the DE 2 satellite [*Winningham et al.*, 1981]. Together, the auroral imagers and the plasma instruments have the potential for providing observations with which to describe the spatial distribution and temporal evolution of the aurora, and to characterize on a global scale the energy fluxes and possibly even characteristic energies of the precipitating auroral electrons. It is these hypotheses that we explore in this study.

This investigation represents the first attempt to combine such global observations with a model of the F region ionosphere for the global ionospheric studies. In Section 2 we construct a global model for the auroral oval using the

TABLE 1. DE 1 Auroral Imager Visible Wavelength Description

Photometer	Peak Transmission Wavelength, nm	Passband at FWHM, nm	Sensitivity counts/(kR-pixel)
A (visible)	557.8	0.9	2.4
B (visible)	629.97	1.01	2.0
C (VUV)	(123–160)	—	

Dynamics Explorer optical and plasma observations. The problems and limitations encountered in this construction are described. The DE auroral model is then used as an input to the time-dependent ionospheric model developed over the years by Schunk and co-workers [*Schunk and Walker*, 1973; *Schunk et al.*, 1975, 1976; *Schunk and Raitt*, 1980; *Sojka et al.*, 1981a; *Schunk and Sojka*, 1982]. The results of model computations for electron densities at different altitudes are presented and discussed in Section 3. A discussion of how this ionospheric simulation differs from previous ones is presented in Section 4, where we repeat the study using previously developed empirical auroral models in place of the DE auroral model. The successes and difficulties of this approach to global scale dynamic auroral modeling are summarized in Section 5.

2. DE AURORAL MODEL

2.1. Auroral Observations for November 25, 1981

The high-altitude satellite DE 1 obtained continuous sequences of auroral images in time intervals as great as ~ 4 hours along each orbit during the fall of 1981. The satellite is equipped with a spin-scan auroral imager (SAI) that comprises three scanning photometers with off-axis parabolic reflectors as the primary optical elements. Two of these imaging photometers provide global auroral images at visible wavelengths, each utilizing any of 12 filters selected by ground command. The third photometer is capable of auroral imaging at vacuum ultraviolet (VUV) wavelengths with a similar selection of one of its 12 filters. In typical operation, a $30° \times 120°$ image is obtained every 12 min for each photometer. The images are centered in the Earth nadir direction, with the 30° angular width of each image aligned transverse to the plane of satellite rotation and the coplanar satellite orbital plane. A detailed description of the imaging instrumentation has been given by *Frank et al.* [1981].

For the imaging sequence from 0259 to 0535 UT on November 25, 1981, three images were obtained simultaneously every 12 min. Filter passbands for the three images were 557 and 630 nm at visible wavelengths, and 123–160 nm at vacuum-ultraviolet wavelengths. Table 1 lists the calibration data for these three filters. During this period of time, the northern hemisphere auroral oval is in darkness, and hence, the images shown in the top three rows of Plate 1 reveal the entire auroral oval. Universal time is given for the nadir scan lines at 557 and 630 nm; nadir scan lines for the VUV imager occur about 2 min earlier. For the remainder of this paper, the time of the nadir scan is used as the image mean time. The data sequence is taken as DE 1 approaches apogee at ~ 0400 UT. For the C photometer images at VUV wavelengths, the auroral oval and solar illuminated hemisphere are clearly visible. Images at 557 and 630 nm reveal the entire auroral oval, while the intense sunlit hemisphere is suppressed electronically. A separate count

rate color key is shown on the right-hand side of Plate 1 for each photometer. These count rates correspond to the photometer output in counts per 3.4 ms (counts/pixel). Because we intend to maintain the maximum spatial and temporal resolution, the statistical count rate errors are based upon these count rates, as will be discussed later. Values for photometer sensitivity in counts per kilorayleigh (kR) per pixel are provided in Table 1. These conversion factors are based on a pre-flight laboratory calibration.

In Plate 1, rows 4 and 5 show the 557 and 630 nm images mapped into a corrected geo-magnetic (CGM) coordinate system, with emission intensities converted to kilorayleighs using sensitivities given in Table 1. The color bar for the 630 nm images ranges in intensity from 0.5 kR (the photometer sensitivity at the 1-count level) to 10 kR. The higher intensities are observed in the pre-noon and noon sectors of the auroral oval. In sharp contrast, the peak intensities at 557 nm (28 kR) occur in the night sector auroral oval. By comparing simultaneous images at the two wavelengths, it is evident that the morphology of these two emissions is quite different. On the gross scale shown in Plate 1, the 557 nm images identify regions of auroral electron precipitation for which typical electron energies are several to many keV. In contrast, the 630 nm images identify regions of low-energy ($E \lesssim 500$ eV) electron precipitation [*Shepherd et al.*, 1980; *Murphree et al.*, 1983; *Link et al.*, 1983]. Hence, the different wavelength bands lead to general information about the precipitating electrons spectral softness or hardness as well as the energy fluxes [*Rees and Luckey*, 1974]. In this investigation, we interpret the strong 630 nm dayside emissions as being due to low energy ($\lesssim 500$ eV) electrons. Under conditions of strong electron heating ($T_e \gtrsim 5000°$K) in the F region, significant 630 nm emissions can be produced [*Robinson et al.*, 1985]. This latter mechanism is not considered as a source for 630 nm emissions in this study. The VUV images produce an auroral distribution which closely parallels that associated with the 557 nm images (compare rows 1 and 2 in Plate 1). There are relative changes in the VUV to 557 nm intensity ratios. These changes are discussed later when inferences about the precipitating electron fluxes are made.

A number of auroral features are evident from the images of Plate 1. The spatial area of the aurora changes considerably in the 2.5-hour study period; these changes are quite rapid. Row 4 of Plate 1 shows how the 557 nm emissions change. In the first image (panel 1) a wide emission region is observed in the evening sector extending from 58° to 76° at 2100 MLT. Thirty seven minutes later, it extends from 62° to 70°, and after an additional 48 min it extends from 61° to 82°. Around this later time (0429 UT), a localized area of auroral emissions extends into the polar cap near local midnight. Between the beginning and end of the image sequence the auroral region has changed; initially, it appeared elongated along the 0800-to-2000 MLT direction, while at

TABLE 2. Auroral Boundaries

MLT	Equatorward	Standard Deviation	Poleward	Standard Deviation
0100	62.6	0.7	74.6	5.3
0200	63.0	1.1	75.8	4.8
0300	63.9	0.7	77.5	3.3
0400	65.1	0.8	78.9	3.1
0500	66.2	0.7	79.4	2.1
0600	67.7	1.0	78.3	2.2
0700	69.3	1.6	76.1	2.0
0800	69.9	1.5	76.3	0.7
0900	70.1	0.9	75.0	1.3
1000	70.9	0.4	74.3	1.5
1100	71.5	0.7	73.7	1.4
1200	71.5	0.9	74.0	1.2
1300	71.6	1.2	74.1	0.8
1400	71.1	1.3	73.7	0.7
1500	70.4	1.7	73.4	1.1
1600	68.6	2.3	73.7	1.6
1700	67.0	1.8	73.2	1.7
1800	65.4	1.7	73.1	1.5
1900	64.0	1.5	71.5	1.2
2000	63.3	1.5	70.7	1.9
2100	61.7	1.5	70.3	2.2
2200	60.9	1.1	73.4	4.6
2300	61.0	0.9	73.5	3.4
2400	61.5	0.7	74.2	4.2

The boundary is defined as 2 kR at 557 nm.

the end of the series it is nearly circular. Global auroral dynamics on this scale has never before been available. In this 2.5-hour study period, the bright auroral region's poleward and equatorward boundaries have changed by as much as 10° in latitude (0200 MLT poleward boundary), a distance of more than 1000 km, a dimension more typically associated with the auroral arc east-west length. At other local times the latitudinal displacements are typically ±3°. Table 2 tabulates the mean and standard deviation of the kR equatorward and poleward auroral boundaries as a function of local time for the 557 nm data shown in Plate 1 (row 4). For the purposes of the present study, a level of 2.0 kR at 557 nm is used as the criterion for defining an auroral boundary. Clearly, to an auroral observer this behavior is not surprising; however such quantitative time-dependent variations in the auroral region have never before been available to theoreticians modeling the ionosphere, thermosphere or magnetosphere. With the current global ionospheric and thermospheric models having binning resolutions on the order of 2° to 5° in latitude, these dynamic boundary changes move the entire oval several model bins in the 2.5-hour period. Moreover, for the Lagranian technique used by the time-dependent ionospheric model (TDIM), the spatial resolution during the computations is typically 0.1° to 1° (10 to 100 km), which is equivalent to the pixel resolution. These changes are therefore significant even on the scale of coarse global ionospheric and thermospheric models. It is the purpose of the remainder of this study to try to represent these auroral observations in such a way that global models can use this dynamic information.

Most of the auroral emissions at 630 nm are of very low in-

tensity, the exception being around local noon. This sector is associated with the magnetospheric dayside region, which is characterized by high fluxes of relatively soft auroral electron precipitation [Winningham et al., 1977]. For typical dayside auroral electron spectra, the average energies are below 500 eV. As already stated, we correlate the bright 630 nm emissions with such auroral spectra and subsequently identify this bright extended region as a region of soft precipitation (see Plate 1, row 5). The enhanced levels of 630 nm emissions observed here are probably related to the prior passage of a shock in the interplanetary medium. A sharp increase in the magnitude of the interplanetary magnetic field (IMF) from −6 to 13 nT was observed with ISEE 1 at ∼ 0225 UT. Additional increases to > 20 nT were recorded by ∼ 0245 UT (C. T. Russell, personal communication, 1986). Untimely data gaps in the period ∼ 0350–0430 UT prevented continuous observation of the IMF throughout the full period of interest. However, observations with ISEE 1 and IMP 8 (R. P. Lepping, personal communication, 1986) otherwise show that the field turned strongly northward after passage of the shock and remained northward throughout the period of the DE 1 observations. The auroral morphology displayed by the 630 nm images is drastically different from that of the 557 nm and VUV images. Again this is not unexpected, but again it is a quantitative data base of global auroral dynamics never before available to the theoretical modeling community. How is one to reconstitute this dynamic, spectroscopic, auroral morphology so that a global-scale ionospheric model, such as the TDIM, can use it? In the following sections we outline a first attempt at this task.

2.2. Image Conversion Algorithm

The conversion of auroral images to "images" of the auroral parameters is not a well established procedure (see below), especially when information concerning soft (< 500 eV) precipitating electrons is required. For this initial study, our methodology is to use three different techniques in a hybrid manner to obtain a "best" set of auroral inputs. To proceed we require the following: (1) 12-min time resolution in the auroral oval; (2) complete auroral coverage in the northern hemisphere with high spatial resolution (≈ 100 km × 100 km pixels); and (3) electron energy flux and characteristic energy for each pixel in each image.

The first technique for obtaining model inputs was to obtain a precipitation energy flux and average energy for each image pixel by simultaneous measurements of the intensities at two wavelengths. The second procedure was to compute a global integrated energy flux using the values for the precipitation energy flux and average energy previously determined, and to compare it with a statistically deduced hemispherical power input, and rescale if necessary. This step provided additional confidence in the albedo correction (discussed in the next section). For the third technique, the inferred energy flux and average energy were compared with in-situ DE 2 LAPI observations gained simultaneously. Further details of the three techniques are given in the following paragraphs.

The first step involves the use of spectroscopic auroral observations to infer the nature of the energy sources of the emissions, which in this case are assumed to be precipitating electrons. From ground-based spectroscopic observations the problem of choosing the appropriate chemistry
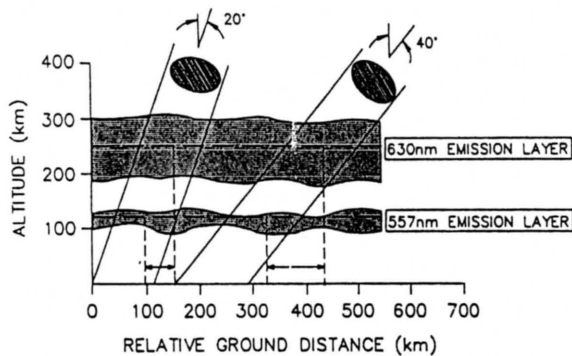
Fig. 1. Schematic representation of oblique DE 1 auroral imager photometer fields-of-view at auroral altitudes for DE 1 apogee conditions. The different emission altitude characteristics are shown via the two shaded regions.

exists in using 630 and 557 nm in addition to geometrical (off zenith observations) and meteorological (atmosphere/cloud effects) difficulties. These difficulties are not changed by using satellite spectroscopic observations. Indeed, additional difficulties surface: integration over larger regions of space ($\sim$ 100 km $\times$ 100 km) and albedo effects. On the other hand, when one considers how crudely current day global-scale ionospheric and thermospheric models incorporate the auroral oval (i.e., a statistical electron precipitation model) it is evident from Plate 1 (rows 1 to 3) that an alternative representation is possible and indeed "morphologically" more accurate. We therefore proceed, identifying as carefully as possible our assumptions and associated geometrical difficulties, to produce an auroral model based upon the DE observations.

2.2.1 *The 557 and 630 nm and VUV conversions.* Ionospheric emissions at different wavelengths provide information not only about different chemical processes, but also about auroral energy sources. For instance, the 630 nm emission can be a signature of soft ($<$ 500 eV) electron precipitation, while emissions at 557 nm and at VUV wavelengths are indicative of precipitation in the 0.5 to 20 keV range. Combining information from two or more wavelengths has the potential of unscrambling auroral parameters. *Rees and Luckey* [1974, and references therein] describe in detail how the auroral energy flux and characteristic energy can be obtained from simultaneous observations of emissions at 428, 557 and 630 nm assuming that the spectral shape is defined. We base our 557-630 nm auroral emission conversion calculations directly on the work of *Rees and Luckey* [1974]. A second emission conversion using 557 nm-VUV is also used (M. H. Rees, private communication, 1987). The question of 630 nm and 557 nm emission chemistry is still controversial [*Link et al.*, 1983; *Rees*, 1984; *McDade and Llewellyn*, 1984; *Langford et al.*, 1985]. However, Plate 1 demonstrates that the use of contrasting wavelengths such as 557 and 630 nm should, in principle, be able to give an indication of the energy flux and also auroral spectral information on a global scale in addition to good spatial and temporal resolution. Here the term "good spatial and temporal resolution" refers only to that currently available to global-scale modelers of the ionosphere and thermosphere.

In the 2.4-hour time interval shown in the plate, the intensity of the emissions changes indicating primarily changes in the electron precipitation intensity. During this time, the 557 and 630 nm emissions are not well correlated, which al-

ludes to different dependencies upon the electron precipitation spectrum. Finally, on a 12-min time period, significant spatial changes of the auroral emission regions are present.

Row 6 in Plate 1 shows the energy fluxes inferred from the images. The twelve "images" are shown in the same format (CGM coordinates) as for rows 4 and 5. For this initial study, small corrections in collocation of pixels for the two different emission altitudes have not been made, but corrections have been made to yield zenith intensities for these optically thin emissions. By using only images obtained near DE 1 apogee and with most of the auroral phenomena being away from the image limb (see Plate 1 rows 1, 2, and 3), the problem of collocation for different emission altitudes is minimized.

Figure 1 shows the pertinent features involved in the collocation of pixels assuming that the 557 and 630 nm photons are ideally emitted in layers centered at 115 [*Jones*, 1974] and 250 km [*Sharp et al.*, 1979], respectively. These altitudes are not unique; they depend upon the auroral conditions; however, they represent a reasonably wide separation of the emission layers leading to a maximized viewing problem. A single pixel at apogee corresponds to a circle of 60 km radius at an altitude of 100 km in the ionosphere. Figure 1 shows how the photometer fields-of-view intersect the ionosphere for zenith angles of 20° and 40°. The respective offsets in horizontal location for the center of the 630 and 557 nm pixels are 70 km (20°) and 180 km (40°). This difference is within the pixel resolution for a 20° zenith angle, while at 40° it is just outside the pixel resolution. Hence, for global imaging purposes the 557 and 630 nm emissions are reasonably collocated. For oblique incidence, a simple cosine correction, based on the assumption of a horizontal emission layer, was used to correct the emission intensities.

A further consideration of how the observed fluxes should be corrected relates to the question of albedo. Since the observations are made from above the auroral emission layer, which has a scattering atmosphere and reflecting earth below it, background emissions are important. The correction for albedo can be greater than 100% of the true emission intensity [see *Hays and Anger*, 1978]. For this initial study, we assumed that the albedo accounts for 50% of the emission (M. H. Rees, private communication, 1986). The albedo correction depends on wavelength, cloud cover, geographic ground conditions and viewing angles relative to nadir. A rigorous calculation is beyond the present work, but it is noted that this adopted albedo may well introduce a factor of two uncertainty.

The energy flux shown in Plate 1 (row 6) is from the 557-630 nm. In addition, the energy flux based upon the more recent auroral algorithm of M. H. Rees (private communication, 1986) using 557 nm and VUV was also used. The two sets of auroral energy fluxes were comparable to within 33% for regions of high fluxes. Statistically, the mean ratio and its standard deviation between the two models were 0.67 $\pm$ 0.05. The Rees and Luckey energy fluxes were smaller than the newer conversion model values. The analysis was performed for only statistically reasonably significant energy fluxes; in other words pixels for the observed photons exceeded 4 at 557 nm. As an indication of the statistics involved, a 557 nm pixel count of 1, 3 or 5 corresponds roughly to an inferred energy flux of 0.5, 1.5 and 2.5 erg/cm^2 s, respectively. In the case where the 630 nm count rate was comparable or higher than the 557 nm, the Rees and Luckey

TABLE 3. Auroral Hemispherical Power Inputs

Image	UT*	DE Model Energy Flux, GW	AE	Integrated Spiro Model Energy Flux GW
1	0305	208	158	60
2	0317	190	139	56
3	0330	171	118	51
4	0342	153	149	58
5	0354	174	198	68
6	0406	154	172	62
7	0418	134	95	43
8	0430	130	120	52
9	0442	146	237	77
10	0454	144	442	111
11	0507	144	496	121
12	0519	126	496	121
		Average		*Average*
		156		73

*On November 25, 1981, northern hemisphere.

energy fluxes were decreased even further. The ratio would then become as low as 0.5. This latter feature is associated with the softening of the auroral spectrum in cases of large 630 nm emission relative to 557 nm in the Rees and Luckey model calculations.

2.2.2. *Hemispherical auroral power input.* Over the past few years, a good correlation has been found between the total or hemispherical auroral power input and auroral indices (D. S. Evans, private communication, 1986). The hemispherical auroral power input is estimated from localized observations of auroral particle precipitation with the NOAA-TIROS satellites [*Evans*, 1987]. Alternatively, from a knowledge of the AE index, the hemispherical auroral power input can be inferred from statistical auroral models, such as the *Spiro et al.* [1982] empirical model. Integration of the auroral energy flux distributions inferred here from optical measurements provides a third method of obtaining a measure of hemispherical auroral power input. We have used and compared the three methods for computing a hemispherical auroral power input.

Table 3 lists for each pair of 557-630 nm images the hemispherical auroral power in gigawatts (GW) after the albedo correction of 50% has been made. Also listed are the AE index and the corresponding hemispherical auroral power input based on the *Spiro et al.* [1982] statistical auroral model. This model is found to be reasonably well correlated with the AE index even though only four ranges of activity are used in the *Spiro et al.* model. The listed AE index has been used to linearly interpolate between the four activity levels in the auroral models. Our inferred hemispherical auroral power inputs are between 1.0 and 3.5 times larger for the 557-630 nm energy fluxes than that obtained by integrating the Spiro et al. empirical model. For the 557 nm-VUV images, they are a further 33% larger.

During the 2.5-hour period, the NOAA 6 and 7 satellites crossed the northern and southern auroral ovals a total of seven times. From the crossings, the power inputs were estimated to range from 21 to 67 GW (D. Evans, private communication, 1986). These values are lower than those computed by either integrating the Spiro et al. or the new DE energy flux models. In either case, it appears that the new energy fluxes deduced from the auroral images

are about a factor of two larger than those deduced by the other two methods, which themselves are not equal. Given all the concerns and uncertainties in using auroral images, the above general consistency in energy flux is good. Ascertaining the error in the image procedure, or how this error depends upon a particular step in the analysis, is exceedingly difficult. Additional corrections, such as albedo and the assumed auroral extent relative to a pixel, could also lead to factors of two error. Indeed, even the Spiro et al. statistical energy fluxes and the NOAA energy deposition calculations are themselves not free of error. Hence, the absolute energy flux has an attached uncertainty comparable to the difference between these techniques, but the major gain is that the DE auroral model gives the dynamics and spatial distribution of the global auroral oval.

In order to proceed with this initial study, we made the following assumptions: (1) The DE auroral model represents the spatial distribution of the auroral oval; (2) the DE auroral model represents the temporal variation of this auroral oval; and (3) the absolute energy fluxes deduced from the images have an associated error. In Table 3, the DE model integrated energy fluxes range from 126 to 208 GW per hemisphere. Considering the level of geomagnetic disturbance, these values are somewhat large. The large difference in absolute energy flux between the DE and Spiro models (Table 3) would hamper the relative comparisons between the two models described in Section 4. Hence, we have reduced the DE model energy fluxes by a factor of two. The effect of the third assumption can, to some extent, be checked by using the in-situ DE 2 LAPI observations (see next section). This model is both temporally and spatially superior to previously available global auroral precipitation energy flux models.

2.3. *Comparison of the LAPI and the Auroral Imager Data*

The low-altitude plasma instrument (LAPI) on DE 2 consisted of 15 divergent parabolic-plate electrostatic analyzers, each of which provided differential spectral measurements of electrons and positive ions over the energy range ~ 5 eV to ~ 30 keV with 1 s temporal resolution. Analyzer fields of view were selected to provide optimal sampling within and
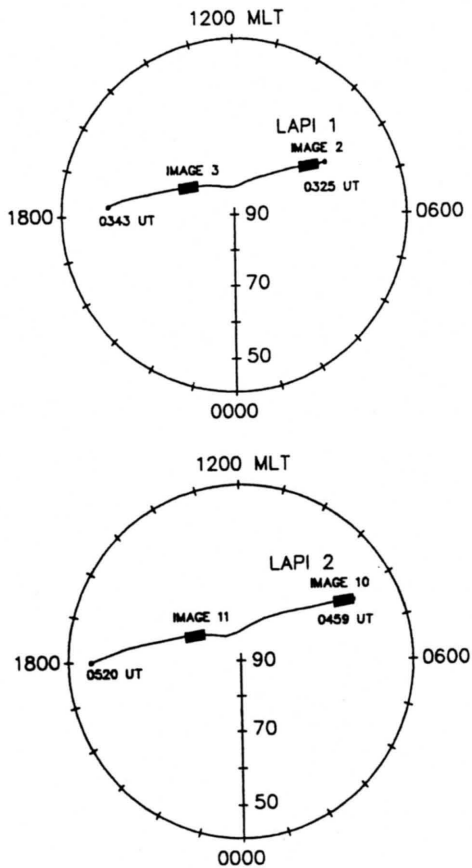
Fig. 2. DE 2 orbit tracks in the CGM coordinates for two northern hemisphere passes (LAPI 1 and 2) on November 25, 1981. The start and end times of these orbit tracks are given in UT. Solid rectangles indicate synchronized DE 1 auroral image pixels and DE 2 LAPI observations. These areas are labelled with an image number corresponding to the image sequence number used in Plate 1.

outside of the source and loss cones at DE 2 altitudes (500–1000 km). For observations on November 25, 1981, 16-point energy spectral measurements were made for particles at pitch angles 0°, 7.5°, 15°, 30°, 45°, 60°, 97.5°, 105°, 112.5°, 135°, 165°, 172° and 180°. Further details and calibration information on LAPI may be found in *Winningham et al.* [1981].

Figure 2 shows the DE 2 sub-satellite track in CGM coordinates for two orbits. The orbits, labelled LAPI 1 and LAPI 2, are approximately dawn-dusk crossings of the northern auroral oval. The start and end times of both satellite tracks are provided. Two images were acquired with each imager during each of the two DE 2 orbit segments. Since the nadir scan line is oriented along the orbit plane of DE 2, auroral intensities and LAPI particle spectra can be obtained nearly simultaneously at one point along the track per image. For the two DE 2 passes the locations of simultaneous DE 1 auroral observations are highlighted (with solid rectangles) in Figure 2. Each solid rectangle is labeled with a number that corresponds to the image numbering scheme shown in Plate 1.

2.3.1. *Energy fluxes.* Figure 3 shows the observed LAPI precipitating electron energy flux (dotted line) for the first orbit (labeled LAPI in Figure 2). The energy flux is the

integral over the 5 to 5000 eV range for precipitating pitch angles. Also shown in Figure 3 are the inferred energy fluxes (solid line) along the DE 2 satellite path for image 2 (bottom panel) and image 3 (top panel). The DE 2 LAPI data are plotted as a function of time. Energy fluxes derived from the imaging data are plotted on the same axis, but the time assigned to each measurement is not the imaging time; it is the time DE 2 crossed the geographic location of the image pixel. In each panel, a vertical shaded region identifies the regions in which the two data sets were obtained simultaneously.

In the 12 min that separate the two images, the auroral energy flux has changed significantly; compare the solid lines in the top and bottom panels of Figure 3. Hence, one should only expect qualitative similarities between these data sets; detailed comparisons can only be made where the two data sets have been obtained simultaneously at the same spatial coordinates (the shaded areas in Figure 3). Energy fluxes determined by the two methods in the dusk sector of the auroral oval at ∼ 0337 UT are quite similar in magnitude and spatial structure. In this shaded region, the energy fluxes agree to within a factor of two. Similar agreement is obtained in the shaded region of the lower panel, where unfortunately the observed auroral intensities are much weaker.
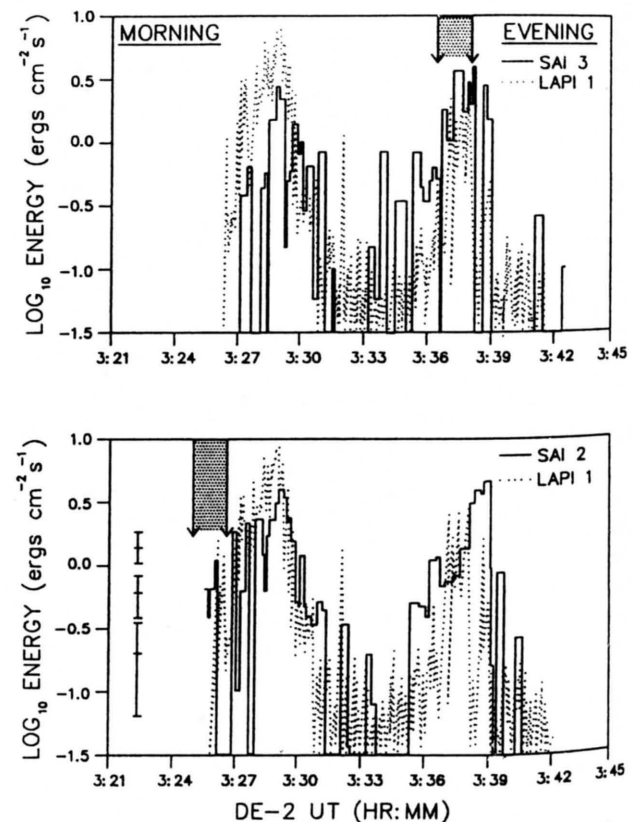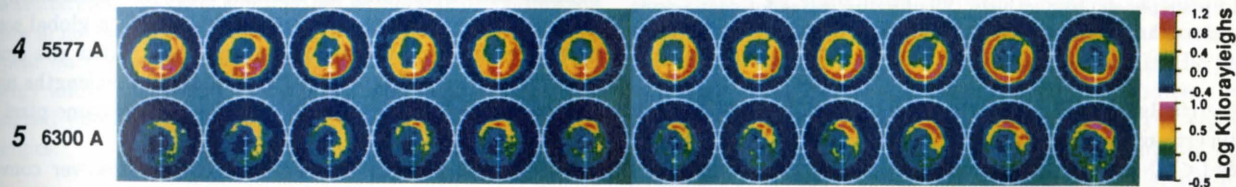

Fig. 3. Auroral energy fluxes (erg cm^{-2} s^{-1}) plotted as a function of UT for the LAPI pass 1 shown in Figure 2, dotted line in both panels. The solid line represents the SAI inferred energy flux along the DE 2 orbit for auroral images 2 and 3 in the lower and upper panels, respectively. Shading indicates for each image where synchronization with the LAPI observations is achieved. In the lower panel, left side, three error bars indicate the statistical accuracy based only upon image pixel count rate statistics.

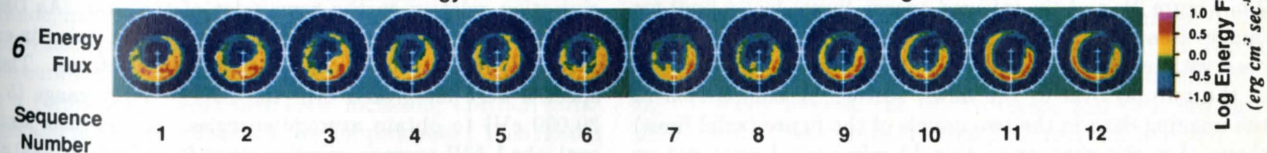**SAI Auroral Image Sequence   25 November 1981**
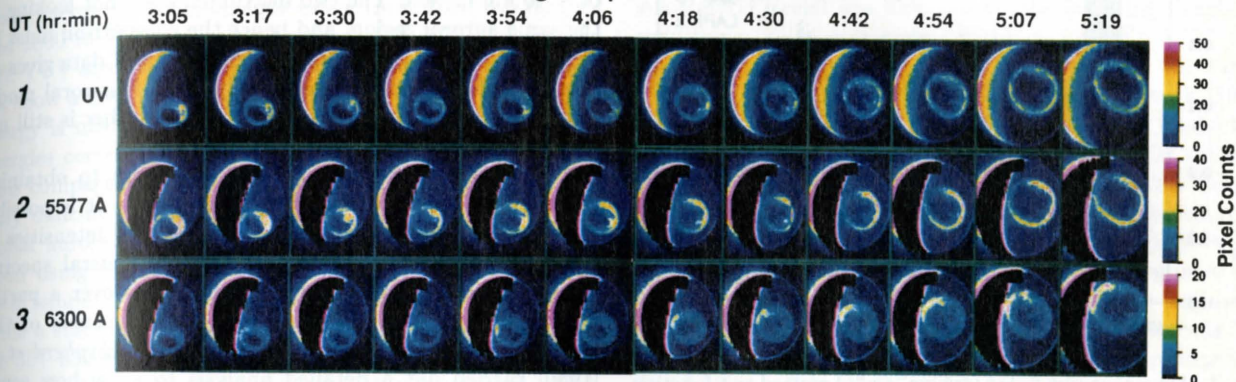
Plate 1. DE 1 auroral image data base for November 25, 1981 from 0259 to 0529 UT. Rows 1, 2 and 3 show, respectively, the UV, 557 and 630 nm images whose count rates have been color coded according to the color scales at the right of each row. In rows 4 and 5 the 557 and 630 nm images have been converted to kilorayleighs and transformed to CGM coordinates. Each dial is a polar plot with latitudinal tick marks at 10° intervals. The circle marks 50° latitude and has hourly MLT tick marks; midnight is at the bottom, 0600 MLT to the right, and noon at the top. The auroral energy flux inferred from these images is shown in row 6. Each row is separately color coded and has its own color key on the right hand side.
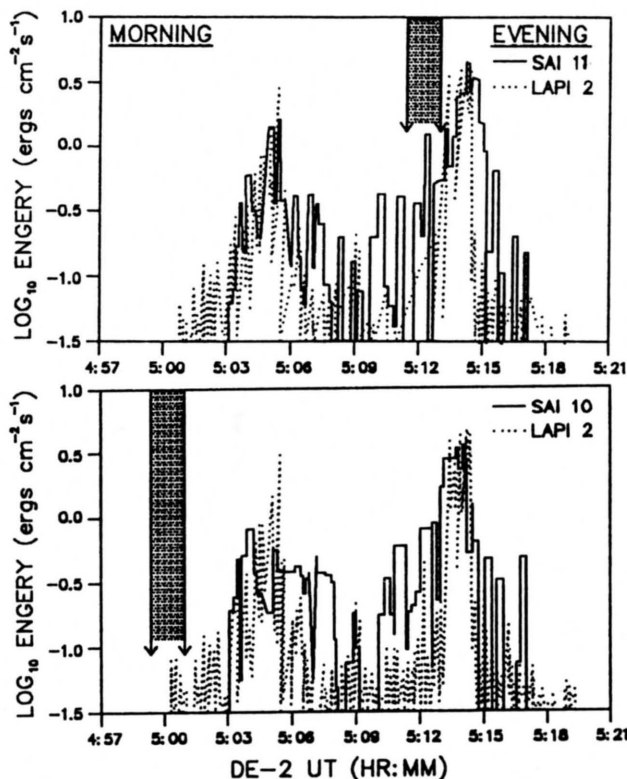
Fig. 4. Auroral energy fluxes (erg cm^{-2} s^{-1}) plotted as a function of UT for the LAPI pass 2 shown in Figure 2, dotted line in both panels. The solid line represents the auroral image inferred energy flux along the DE 2 orbit for images 10 and 11 in the lower and upper panels, respectively. Shading indicates for each image where synchronization with the LAPI observations is achieved.

The error bars in Figure 3 (lower panel) indicate the range of uncertainty in determining the energy fluxes for low count rates (< 20 counts/pixel).

Figure 4 shows the observed LAPI precipitating electron energy flux (dotted line) for the second orbit (labeled LAPI 2 in Figure 2), and the inferred energy fluxes (solid line) for images 10 and 11. Unfortunately, the region of simultaneous observations (shaded area) at ∼ 0500 UT lies equatorward of the auroral oval in the dawn sector. A comparison of the imaging data in the two panels of the figure (solid lines) shows that the changes in this 12 min period were not as marked as for Figure 3. In the absence of significant temporal variation, the overall latitudinal profiles of energy fluxes, as determined with LAPI and inferred from the images, are strikingly similar. Unfortunately, the region of simultaneous observations in the evening sector at ∼ 0512 UT was located at the poleward edge of the auroral oval, which is a region of large gradients in the energy flux as a function latitude. For our present purposes, the large-scale spatial and temporal auroral variations that we infer from the SAI images are consistent with the high resolution LAPI observations. Quantitatively, the inferred energy fluxes are within a factor of two to three of the LAPI energy fluxes when the latter are larger than 0.5 erg/cm^{2}s.

The use of these two LAPI passes by no means constitutes a statistically significant verification of the DE auroral model. During the 15-min DE 2 time segments over the northern auroral region, the auroral dynamics are significant (compare Plate 1 images 2 with 3 and 10 with 11).

This LAPI comparison is used as a further means of checking the self-consistency of the inferred energy fluxes. In both Figures 3 and 4 the auroral oval sections, as seen by LAPI and as inferred, are similar but not the same. Whether the differences are primary temporal effects or due to the image interpretation analysis cannot be resolved, but they do confirm that the two techniques yield comparable (to a factor of ∼ 2) energy fluxes. These results are also consistent with other image-LAPI comparisons (M. H. Rees, private communication, 1987). In carrying out this comparison, a much more severe difficulty is alluded to; namely a single 3.4 ms image pixel covers a region ≃ 100 × 100 km, whereas each LAPI spectral sweep spans a DE 2 satellite track distance of ∼ 10 km or less. The two instruments are not looking at the same auroral region, and hence the comparison must be treated cautiously. Using the image and LAPI data gives an overall confidence that qualitatively the DE auroral model is reasonable; however, the absolute energy flux is still uncertain to the degree described earlier.

2.3.2. *Characteristic energy.* In addition to obtaining the energy flux from the DE auroral images, it is possible to obtain spectral information. The ratio of intensities at different wavelengths is indicative of the general spectral shape of the auroral precipitating electrons over a particular energy range. Unfortunately, the uniqueness of this spectroscopic inversion is not well defined. *Shepherd et al.* [1980] carried out a detailed analysis to show how sensitively the photon emission fluxes at different wavelengths depend on the auroral spectral shape. From this study it is evident that describing an auroral electron spectrum by a single energy parameter is very difficult. On a global scale this question becomes even more complex, since the emission regions associated with two different wavelengths may not be identical even though they refer to the same pixel (a region ∼ 100 × 100 km).

Looking at the images in Plate 1 does however convey qualitative information on the auroral spectrum. The extended dayside oval is bright in 630 nm, indicating soft precipitation relative to the remainder of the oval. As DE 2 crosses these images (see Figure 2), LAPI obtains in-situ spectral information of the precipitation electrons. These spectra were integrated over the LAPI energy range (5 to 30,000 eV) to obtain average energies. In the dusk sector oval, the LAPI average energies range from 1000 to 3000 eV, while in the noon-morning oval, the average energy ranges from 2500 to 6000 eV. These average energies imply a harder spectrum in the noon-morning sector than the dusk sector, which is contrary to our expectation. The noon-morning sector spectra, however, were complicated. They contained a soft (< 1 keV) component superimposed on a hard power law (10 keV) spectrum. Hence, as *Shepherd et al.* [1980] found, it is exceedingly difficult to derive a single parameter. The integration over the electron number flux should fold in a weighting function representative of how efficiently the desired photons are produced at each energy.

From the image data and the *Rees and Luckey* [1974] and M. H. Rees (private communication, 1987) image conversion algorithms, a characteristic energy is also obtained. Assuming, as is the case for these model calculations, that the electron spectrum is Maxwellian, these characteristic energies are half the corresponding average energy of a Maxwellian population [*Robinson et al.*, 1987]. Auroral spectra are not,

in general, well represented by Maxwellian distributions, and consequently, the Maxwellian assumptions contained within the conversion algorithms will introduce an error in comparing characteristic and average energies. Unfortunately, this error is not readily quantifiable. For the present purpose, the energy is only used to indicate the spectra hardness of the precipitation. In using the DE auroral model, the ionosphere responds more strongly to the energy flux than to the average energy. In the dusk sector, the images yield equivalent average energy values of 2000 to 5000 eV and 1000 to 3000 eV, respectively, for the 557–630 nm and 557–VUV algorithms. These values are in the same range as obtained in-situ by LAPI. In the morning sector, the equivalent average energy from the images range from 1000 to 6000 eV and 1000 to 3000 eV, respectively, for the 557–630 nm and 557–VUV algorithms. As already discussed, the LAPI spectra show a double component and consequently the average energy is misleading. In the case of the images, the lower energies correspond to regions of strong 630 nm emission. This comparison, although favorable numerically, is physically difficult to quantify. However, the state-of-the-art in global auroral modeling can to some extent be improved upon using these algorithms because they do respond to both temporal and spatial changes in auroral morphology, while a statistical model cannot. For this study we will use the 557–630 nm inferred average auroral energies (see Plate 2, row 4). These energy images are highly structured, which reflects the difficulty in using ratios of single pixels whose count rates are low. Much of the structure is associated with the statistics. However, when either or both pixel counts fell below 3, no energy calculation was performed. These regions appear on the color plots as the background color. When energy information for these regions was needed they were assigned energies by averaging the nearest non-zero pixel energies.

3. IONOSPHERIC MODEL

The ionospheric model was initially developed as a mid-latitude, multi-ion (NO^+, O_2^+, N_2^+, and O^+) model by *Schunk and Walker* [1973]. The time-dependent ion continuity and momentum equations were solved as a function of altitude for a corotating plasma flux tube including diurnal variations and all relevant E and F region processes. This model was extended to include high latitude effects due to convection electric fields and particle precipitation by *Schunk et al.* [1975, 1976]. A simplified ion energy equation was also added, which was based on the assumption that local heating and cooling processes dominate (valid below 500 km). The trajectories for plasma motion were determined as the plasma moved in response to convection electric fields. A further extension of the model to include the minor ions N^+ and He^+, an updated photochemical scheme, and the mass spectrometer/incoherent scatter (MSIS) atmospheric model is described in *Schunk and Raitt* [1980].

The addition of "constant" plasma convection and empirical models for particle precipitation is described in *Sojka et al.* [1981a, b]. More recently, the ionospheric model has been extended by *Schunk and Sojka* [1982] to include ion thermal conduction and diffusion-thermal heat flow, so that the ion temperature is now rigorously calculated at all altitudes between 120 and 1000 km. The adopted ion energy equation and conductivities are those given by *Conrad and*

Schunk [1979]. Also, time-dependent plasma convection and particle precipitation inputs have been used with the basic high-latitude model so that magnetospheric storm and substorm conditions could be studied [*Sojka and Schunk*, 1983, 1984].

3.1. Initial F Region Conditions

For this study we used the high-latitude storm model inputs [*Sojka and Schunk*, 1983, 1984] to simulate the F region response to the observed auroral dynamics. A time-dependent study requires a pre-computed set of appropriate initial ionospheric densities. Such information is not empirically or observationally available. Consequently, the ionospheric model was first run for the following simplified conditions: solar maximum ($F10.7 = 150$), $Kp = 2^+$ and $Ap = 9$ (conditions appropriate for November 24, 1981). The auroral conditions were based upon a *Spiro et al.* [1982] average oval for an $AE = 200$ and the convection model had a cross-tail potential of 48 kV with a symmetric Volland-type pattern (see *Sojka et al.* [1981a] for further details concerning these inputs). These conditions were approximately suitable for November 24, 1981, the day prior to the study day. However, significant activity had begun in the 3-hour period of November 25 just prior to the beginning observation used here. Kp for this 3-hour period was 5^-. Since the starting conditions were not entirely appropriate, the absolute values of the modeled densities must be treated with caution. Beginning with the above initial conditions, the time-dependent inputs to the ionospheric model were then driven by the auroral dynamics defined by the image sequence described in Section 2. At this time, the study period convection pattern also had to be defined. In the past, all of our model studies have used magnetic indices, such as Kp or the IMF (B_x, B_y, B_z), to determine the convection pattern [*Sojka et al.*, 1981a, b, c]. For a study as short as 2.5 hours, only a single Kp value is available; unfortunately, between 0300 and 0600 UT the ISEE 3 IMF data had a gap. Prior to the first image, the IMF B_z was southward with a value of -3 nT, but after the last image (0529 UT) it was northward with a value of almost 20 nT which was then maintained for many hours. In other words, during our study interval the IMF reversed and went strongly northward. It was probably this IMF reversal that was responsible for the auroral dynamics shown in Plate 1.

At the present time, the information about the convection electric field is not adequate to model it during dynamic periods such as that discussed here. Hence, we approximate the convection pattern during this dynamic 2.5-hour period with a two-cell convection pattern with a cross-tail potential of 80 kV. This convection model is the same as for the quiet conditions described earlier, except that the magnitudes of the electric fields are about twice as great, which is consistent with the change in Kp. Figure 5 shows the adopted magnetospheric convection pattern in the MLT-magnetic latitude coordinate system. The contours are of electric potential in kV. The pattern is centered at 85° magnetic latitude on the midnight meridian. This pattern is then combined with a co-rotational electric potential to give the electric field that drives the plasma convection. For the MSIS neutral atmosphere model parameters, $Ap = 27$ and F10.7=150 were adopted. A simple 200 m/s anti-sunward neutral wind was adopted for the dark auroral polar regions.
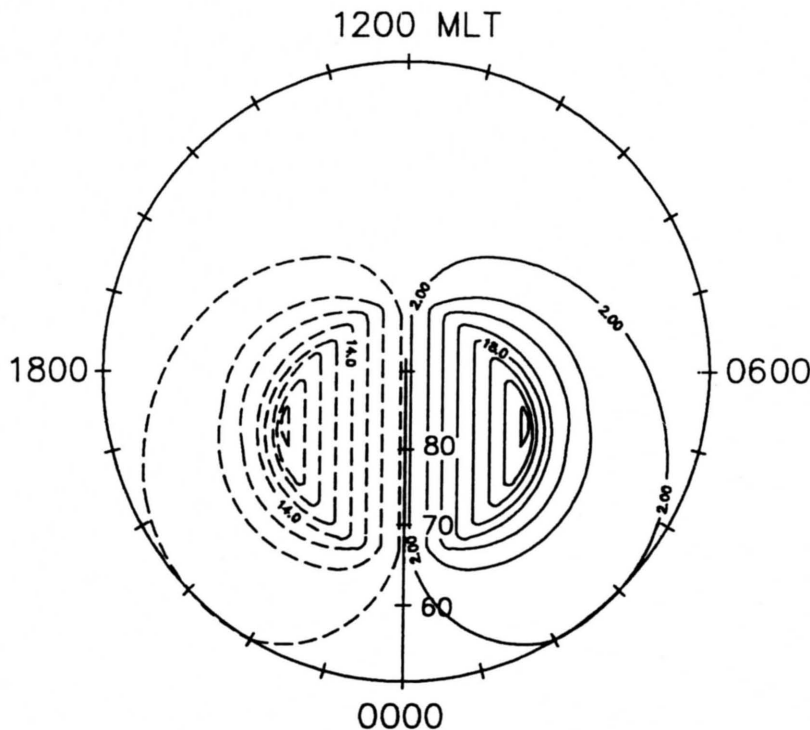
1200 MLT

Fig. 5. Contours of the convection electric potential in a CGM polar diagram. The potentials are contoured at 4 kV intervals.

3.2. High Latitude F Region Densities

The time-dependent convection and precipitation inputs were run for 2.5 hours, starting at 0300 UT on November 25, 1981. Density profiles were computed every 1–3 min along 40 trajectories. Plate 2 shows the computed electron densities at 160, 300 and 800 km for each image time; see rows 3, 2 and 1, respectively. In Plate 2, row 5 shows the energy fluxes inferred from the DE auroral images before the factor of two reduction was introduced (same as row 6 of Plate 1). Row 4 shows the characteristic energy computed from the images. These energies range from $\sim$ 200 to 5000 eV. The lowest energies are found in the cusp (in particular, see images 9 through 12 in the 0900 to 1300 MLT oval region). Both the energy flux and characteristic energy are used as inputs to the calculation of auroral ionization rates, which is based on the production rate profiles of *Knudsen et al.* [1977].

The electron density (N_e) at 160 km varies in a manner very similar to that of the auroral energy flux (compare rows 3 and 5). At 160 km, the highest densities, region color-coded pink in row 3, closely follow the changing region of $\gtrsim 1$ erg cm^{-2}s^{-1} electron precipitation. Even during the period when the night sector polar cap suddenly develops bright auroral structures (images 7, 8 and 9), the electron density at 160 km is enhanced. This one-to-one dependence is expected in so far as the bottomside F region is basically in a state of chemical equilibrium. The chemical time constants are of the order of seconds to at most a minute. Hence, the density responds rapidly to changes in the production rates resulting from changes in the auroral precipitation energy flux. N_e also responds to production due to solar EUV radiation (see low latitudes about noon in row 3). For this study period, the winter terminator lies well equatorward of the dayside oval (see Plate 1, row 1).

At 300 and 800 km, the electron density morphology does

not track the auroral energy flux (compare rows 2 and 1 with row 5 in Plate 2). This decoupling arises from the dominance of horizontal plasma transport and field-aligned diffusion over chemistry at these higher altitudes (see, for example, *Sojka and Schunk* [1984]). One of the main objectives of this study is to quantify the way in which the global-scale F region responds to auroral dynamics. Hence, a detailed comparison of the density variations at 300 and 800 km to the auroral energy flux variations will enable this question to be addressed. At 300 km and auroral oval latitudes (row 2, Plate 2), the N_e maximum value increases by a factor of $\sim$ 2 over the 2.5-hour period. For image 1, the highest N_e densities are found in the sunlit region equatorward of the dayside oval. In contrast, for image 12, at the end of the period, the highest densities are found in the night sector auroral oval (row 2, Plate 2, first and last dials).

The N_e variation at 800 km over this 2.5-hour period is also significant. For both of these altitudes, the polar-cap morphology shows distinct similarities. In the first image the densities are primarily related to the initial conditions (see image 1 of rows 1 and 2 in Plate 2). On the duskside of the polar cap, a well-defined "tongue" of ionization is present, extending from noon, past the pole to midnight. This feature is associated with the plasma convection, which carries high-density noon sector plasma through the cusp region and then antisunward over the polar cap. This feature is highly UT (longitudinally) dependent and has been previously modeled [*Knudsen et al.*, 1977, *Sojka et al.*, 1981c] and observed [*de la Beaujardiere et al.*, 1985]. In the dawn sector, a density depletion exists on the nightside between 80° and 90° latitude. This "polar hole" region is associated with "dark" noon sector trajectories moving through the cusp and across the polar cap. These trajectories initially have low densities (see the pre-noon region between the oval and solar illuminated region in Plate 2, rows 1 and 2, image

TABLE 4. Studies Using Different Auroral Models

Study	Description	Temporal Dependence
1	DE auroral model	12 min resolution using DE 1 auroral image sequence
2	*Spiro et al.* [1982], variable	12 min resolution using AE* index
3	*Spiro et al.* [1982], fixed	none, AE index fixed at 496

*The AE variation is given in Table 3, column 4.

1). In crossing the cusp region, the plasma density is only slightly enhanced and then decreases as the plasma moves antisunward over the polar cap.

In the 2.5-hour duration of the study, the corresponding N_e features associated with "time-independent" convection and precipitation patterns would remain unchanged. However, by image 12 in Plate 2 both the "tongue" of ionization and the "polar hole" have changed markedly. The polar hole has moved about 10° more antisunward, while the tongue of enhanced ionization blends into a generally enhanced dusk sector polar cap. These changes are associated with the systematic variation in auroral precipitation and convection speed, both of which have approximately doubled in going from pre-0300 UT to the study period, 0300–0530 UT.

Although at both 300 and 800 km, a density enhancement in the form of an auroral region is present, it is not similar to the spatial distribution of the aurora and large energy fluxes (compare rows 1 and 2 with row 5 in Plate 2). This is most apparent in the 0700 to 1200 MLT sector where the precipitating energy flux is small ($\lesssim 0.3$ erg/cm^{2}s). In this region, at both 300 and 800 km, N_e is relatively high over a very wide region. N_e is not high in this region at 160 km altitude, which implies there is no bottomside production source. These high densities, which occur in a dark region, are generated and maintained by local "soft" electron precipitation and plasma transport from the post midnight auroral region.

The effect that the arbitrary factor of two reduction in energy flux in the DE model has on the plasma density depends upon altitude. At low altitudes, ~ 160 km, the density scales approximately as the square root of the energy flux. Consequently, the factor of two reduction would be associated with a 1.4 density reduction over the entire oval. At higher altitudes, due to the increased role of transport, such a simple scaling does not occur. With typical F region time constants of the order of tens of minutes to hours, the factor of two energy flux reduction could, for certain plasma flux tubes located in the auroral oval, have a similar 1.4 density reduction. Other plasma flux tubes, whose temporal history is more dependent on dayside production and plasma recombination in darkness, will have a significantly smaller density reduction. The shape of F region plasma features will only be slightly modified, i.e., the dynamic ranges of plasma density features in rows 1 and 2 of Plate 2 are 1.5 and 1.6 orders of magnitude, respectively. Hence, a change of less than 2 (0.3 on the log scale used in Plate 2) would be quite small.

4. COMPARISON OF AURORAL PRECIPITATION MODELS

In this section a direct comparison will be made between the auroral model inferred from the DE data and that commonly used in global ionospheric and thermospheric modeling, i.e., the *Spiro et al.* [1982] energy flux model. The comparison enables us to assess how large-scale auroral dynamics represented by these models affects the ionosphere. The *Spiro et al.* [1982] model is based on Atmospheric Explorer precipitating electron data binned into four levels of magnetic activity. *Spiro et al.* [1982] found that the best magnetic activity correlation of the precipitation data was with the AE index. For this 2.5-hour study period, the AE index is available [*World Data Center C2 for Geomagnetism*, 1984]. For our previous long-term studies (i.e., diurnal), we selected and then kept constant a particular level of magnetic activity. This was usually defined by the daily average of the three-hourly Kp index. To contrast the varying and constant auroral oval cases, we ran the ionospheric model with two different Spiro et al. precipitation models. The first (study 2) allowed the AE index to vary with time over the 2.5-hour study period, while the second (study 3) was for a fixed AE value. Apart from the differences in auroral precipitation, the two additional ionosphere runs are identical to that described in Section 3.2 using the DE auroral model. Table 4 lists the differences between the three auroral models. AE activity levels used in run 2 are specified in column 4 of Table 3.

The general results of Section 3.2 are also found to apply to studies 2 and 3: At 160 km, N_e varies with the energy flux, while at 300 and 800 km a marked difference between N_e and the energy flux variations is found. Hence, we will focus on the density at 300 km to compare the studies, since at 160 km the differences are merely given by the differences in energy fluxes. Plate 3 shows the 12-image sequence of N_e "images,' at 300 km for the three ionospheric runs (rows 1, 2 and 3). Rows 4 and 5 show the auroral energy flux model, with row 5 corresponding to the time-dependent AE Spiro et al. model used in run 2, while row 4 is the auroral model inferred from DE (same as Plates 1 and 2, bottom row). For run 3, which used a constant AE Spiro et al. model, the energy fluxes are identical to those shown in image 12 in row 5 of Plate 3.

Neither the time-dependent AE nor the AE-fixed Spiro et al. model resemble the DE auroral model (compare rows 4 and 5 in Plate 3; note that the DE model is the same as in Plates 1 and 2 prior to being reduced by a factor of two). Variations in the spatial distribution of aurora, which are most marked in the DE auroral model between the first and last images, are not reproduced in the statistical Spiro et al. model. In attempting to allow the Spiro et al. oval to change with the AE index (row 5), the energy fluxes undergo much larger variations than are present in the DE auroral model. Image 1 shows the DE auroral oval to be about three times wider than the Spiro et al. oval, while the reverse is true for image 12, a mere 2.5-hours later. The differences are not entirely unexpected, since the study period was selected because of the marked auroral dynamics in a 2.5-hour period. However, the comparison of rows 4 and 5 quantitatively demonstrates how difficult it is to use auroral indices and statistical models to represent specific cases. The consequences of the factor of two uncertainty in absolute energy flux in the DE model would not change these conclusions about spatial differences.

For all three studies (Plate 3, rows 1, 2 and 3), the electron density at 300 km shows similar large-scale variations, although the energy fluxes vary. High densities in the noon
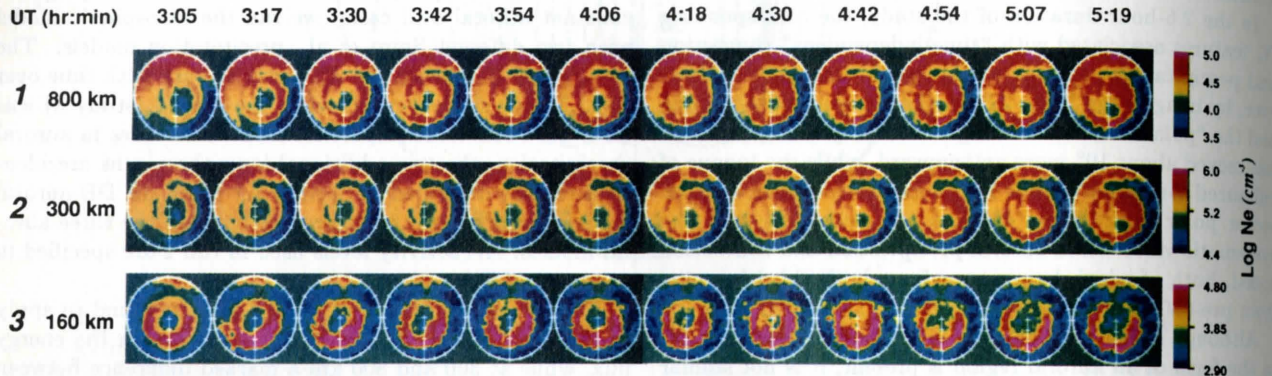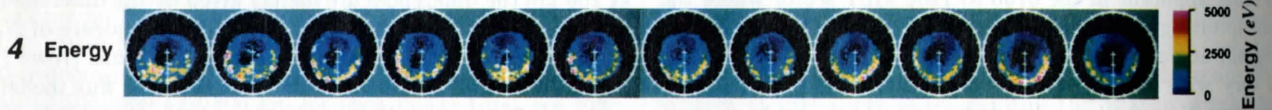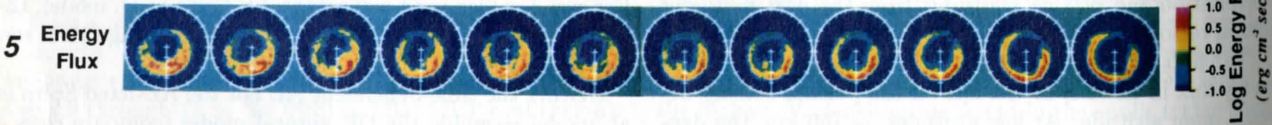
Plate 2. Modeled *F* region electron densities at 160, 300 and 800 km for the 12 image times and color coded in CGM polar coordinates (rows 3, 2, and 1, respectively). Rows 4 and 5 show the DE auroral model average energies and energy fluxes (prior to being reduced by a factor of 2), respectively. For each row a separate color key is given on the right. Each dial is defined in the same way as for Plate 1, rows 4, 5 and 6.

Computed Electron Densities at 300 km for Three Auroral Models
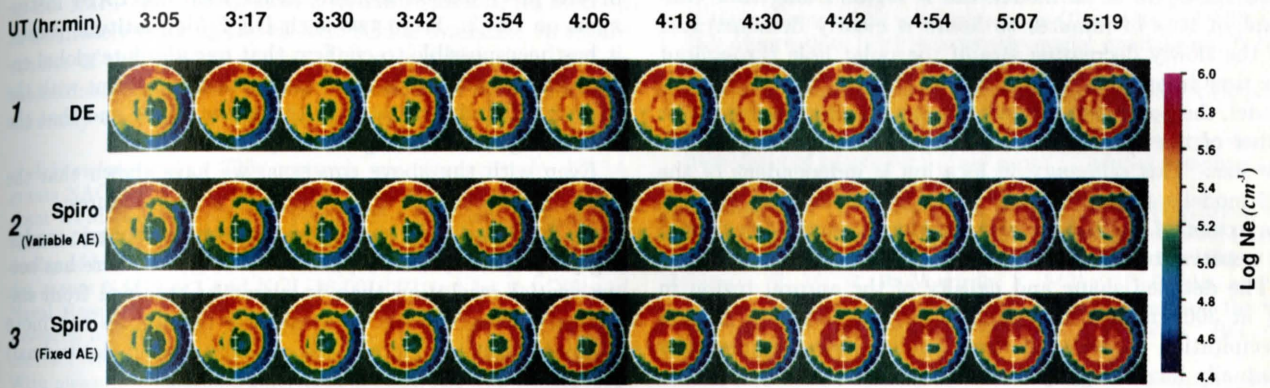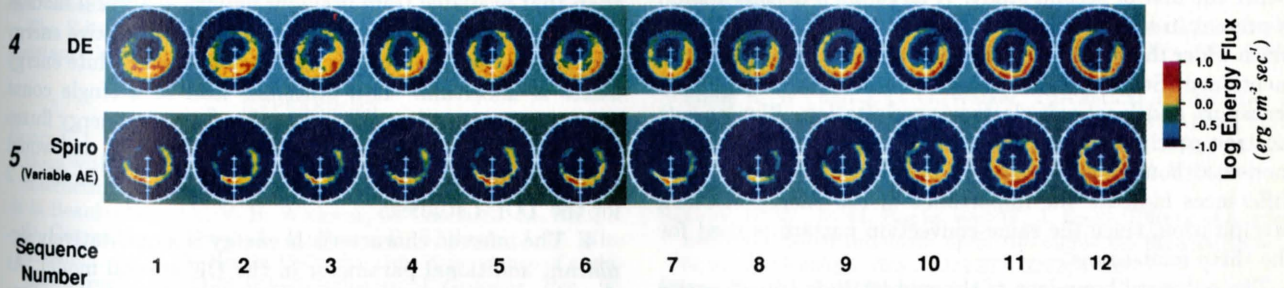
Plate 3. Modeled F region electron densities at 300 km for the three studies listed in Table 4 (rows 1–3). Rows 4 and 5 show the DE auroral model (the energy flux has not been reduced by a factor of 2) and variable *Spiro et al.* [1982] energy fluxes, respectively. For each row a separate color key is given at the right. Each dial is defined in the same way as for Plate 1, rows 4, 5 and 6.

sector region equatorward of the auroral region are, as expected, identical. All three studies also show the "cusp gap", which is associated with low density plasma equatorward of the auroral oval, but in the dark hemisphere, convecting rapidly through the cusp into the polar cap. These low density plasmas are responsible for the formation of the polar hole. The polar hole, found for this study in the morning polar cap, is different for the three runs. Since all inputs to the ionosphere model, except for the auroral models, are identical for these studies, the different plasma density distributions within the polar cap arise from differences in the auroral models. For the time-dependent AE Spiro et al. model, the shape of the polar hole changes significantly (Plate 3, row 2). Images 4 and 12, respectively, demonstrate the extremes of a large and a negligible polar hole. In the fixed AE Spiro et al. model, the F region's long time constant of tens of minutes to hours is clearly demonstrated by the slowly decreasing size of the polar hole throughout the time interval (from frame 1 to 12). For the DE auroral model, the polar hole extends 5° more equatorward than for either of the Spiro et al. models, as well as being double the size. This difference in location is independent of the DE model's absolute energy flux. Other features, such as the extent of the tongue of ionization around noon, would be sensitive to the absolute energy flux.

The detailed shape and density of the auroral region in N_e at 300 km is also dependent on the choice of auroral precipitation model. All three studies show the densities gradually increasing, by about a factor of two over the 2.5-hour period. By the end of the 2.5-hour period, the AE-fixed Spiro et al. model yields a large region of high densities in the post-noon sector. There is no counterpart to this region in either the first or second study. A large, high-density region is present in the pre-noon sector for the DE-study, which is much wider than found in either of the other two. As already mentioned (Section 3), this is a result of horizontal plasma transport and local soft electron precipitation. Similar soft electron precipitation regions are present in the Spiro et al. model, although the average energies are not as low. The differences indicate the importance of low-energy electron precipitation, since the same convection pattern is used for the three model runs.

The poleward boundary of the mid-latitude trough varies between the three models. In the color figures shown in Plate 3, this feature is difficult to see because of the binning resolution (3° in latitude and 1 hour in MLT). Only in the afternoon sector is it evident that the trough poleward edge has different densities for the three studies and, consequently, different latitudinal gradients. Study 3 (the fixed Spiro model) displays a strong gradient on the poleward edge of the trough at all times. In contrast, the second study shows a negligible gradient for most of the study. Both of these variations are different from that found for the DE model. Such temporal variations are indicative of the storm morphology and would be weakly affected by the overall absolute energy flux.

5. SUMMARY

In constructing the DE auroral model, we have for the first time attempted to describe, with both high temporal and spatial resolution, the energy flux and characteristic energy of electrons precipitating into the northern auroral oval.

The construction of this model utilized the DE 1 auroral images at two visible wavelengths (557 and 630 nm) and one VUV wavelength range. The high altitude emissions at 630 nm (180–260 km) and the 557 nm emissions below 180 km are, respectively, indicative of soft ($\lesssim$ 500 eV) and hard ($\gtrsim$ 1000 eV) auroral electron precipitation. When viewed from several Earth radii above the ionosphere, the reconstruction of the emission features leads to problems (see section 2). We have attempted to evaluate these problems by using two additional methods for obtaining the auroral energy flux parameter. The global auroral energy flux was integrated and compared with the statistically expected auroral power input. This procedure showed that our derived global energy flux was a factor of 1 to 3 larger. In addition, the DE program had the unique capability of making in-situ precipitation measurements with the LAPI instrument on DE 2. From two such DE 2 high latitude passes, it has been possible to confirm that our absolute global energy flux model was in good qualitative agreement with the in-situ LAPI observations to the above factor and that the relative agreement is significantly better.

Even with the above concerns, we have shown that the DE auroral model does contain several new features:

1. For large-scale ionospheric and thermospheric modeling purposes, the DE auroral model described here has better spatial resolution than is currently obtained from statistical auroral models. The auroral boundaries can move by more than the global-scale model's spatial (latitudinal) resolution and are consequently significant.

2. Similarly, the temporal resolution of auroral features (dynamics) is unique. Even if 12 min is long on the time scale of an auroral break-up, it is orders of magnitude better than that available from previous empirical auroral models.

3. We have been able to obtain very good relative energy flux variations; however the accuracy of the absolute energy fluxes is uncertain. Low statistics lead to a single count equivalent energy flux of $\sim$ 0.5 erg/cm^2 s. The energy fluxes deduced from the images were larger than what one would expect; hence we reduced the energy fluxes by a factor of 2 for the TDIM studies.

4. The inferred characteristic energy is a qualitatively significant additional parameter in the DE auroral model. At the present time, the characteristic energy is a good qualitative indicator of the hardness or softness of the precipitation.

Using the DE auroral model, a high latitude F region simulation was performed. This simulation was compared to a simulation using the conventionally adopted Spiro et al. [1982] auroral model. Since the auroral image sequence is highly dynamic, this study is the first high-time resolution simulation of the high latitude ionosphere. From these simulations, the following conclusions are drawn:

1. The bottomside F region is coupled to the auroral dynamics on time scales of less than a minute. However, the electron density changes are not simply proportional to the energy flux. Electron density approximately varies as the square root of the energy flux. The auroral boundaries obtained from the images are drastically different from those associated with statistical models. This leads to different conductivities.

2. Near the F region peak and topside, the electron density does not respond on the image time scale to auroral precipitation changes. The density at 300 km responds on

a longer time scale ($\gtrsim$ 30 min). At 800 km, the even longer time scales somewhat but not completely integrate over the short term auroral dynamics.

3. One of the major results of this study is that it shows on a global scale that realistic auroral spatial and temporal variations are significant in the F region where long time constants might have been expected to integrate (smooth) out such variations. F region boundaries are displaced by as much as 5° when compared to those for a comparable statistical oval. The associated electron densities can differ by as much as a factor of 4.

Item 3 clearly implies the need to carry out a comparison between modeled densities and observed densities. Unfortunately, this study period, although ideal from the image point-of-view, is associated with a period of dramatic change in the IMF, and during such a dynamic period, no method of accurately defining the electric field is available. In future studies of this type it is crucial that a well defined IMF is maintained during the period of interest. The authors are currently working on such a follow-up study.

REFERENCES

Conrad, J. R., and R. W. Schunk, Diffusion and heat flow equations with allowance for large temperature differences between interacting species, *J. Geophys. Res.*, *84*, 811–822, 1979.

de la Beaujardiere, O., V. B. Wickwar, G. Caudal, J. M. Holt, J. D. Craven, L. A. Frank, L. H. Brace, D. S. Evans, J. D. Winningham, and R. A. Heelis, Universal time dependence of nighttime F region densities at high latitudes, *J. Geophys. Res.*, *90*, 4319–4332, 1985.

Evans, D. S., Global statistical patterns of auroral phenomena, in *Quantitative Modeling of Magnetosphere-Ionosphere Coupling Processes*, pp. 325–330, Kyoto Sangyo University, Kyoto, Japan, 1987.

Frank, L. A., J. D. Craven, K. L. Ackerson, M. R. English, R. H. Eather, and R. L. Carovillano, Global auroral imaging instrumentation for the Dynamics Explorer mission, *Space Sci. Instrum.*, *5*, 369–393, 1981.

Fuller-Rowell, T. J., D. Rees, S. Quegan, R. J. Moffett, and G. J. Bailey, Interactions between neutral thermospheric composition and the polar ionosphere using a coupled ionosphere-thermosphere model, *J. Geophys. Res.*, *92*, 7744–7748, 1987.

Hardy, D. A., M. S. Gussenhoven, and E. Holeman, A statistical model of auroral electron precipitation, *J. Geophys. Res.*, *90*, 4229–4248, 1985.

Hays, P. B., and C. D. Anger, Influence of ground scattering on satellite auroral observations, *Appl. Opt.*, *17*, 1898–1903, 1978.

Heelis, R. A., J. K. Lowell, and R. W. Spiro, A model of the high-latitude ionospheric convection pattern, *J. Geophys. Res.*, *87*, 6339–6345, 1982.

Heppner, J. P., and N. C. Maynard, Empirical high-latitude electric field models, *J. Geophys. Res.*, *92*, 4467–4489, 1987.

Jones, A. V., *Aurora*, D. Reidel, Hingham, Mass., 1974.

Knudsen, W. C., P. M. Banks, J. D. Winningham, and D. M. Klumpar, Numerical model of the convecting F_2 ionosphere at high-latitudes, *J. Geophys. Res.*, *82*, 4784–4792, 1977.

Langford, A. O., V. M. Bierbaum, and S. R. Leone, Auroral implications of recent measurements on $O(^1S)$ and $O(^1D)$ formation in the reaction of N^+ with O_2, *Planet. Space Sci.*, *33*, 1225–1228, 1985.

Link, R., J. C. McConnell, and G. G. Shepherd, An analysis of the spatial distribution of dayside cleft optical emissions, *J. Geophys. Res.*, *88*, 10145–10162, 1983.

McDade, I. C., and E. J. Llewellyn, A comment on proposed mechanisms for the excitation of $O(^1S)$ in the aurora, *Planet. Space Sci.*, *32*, 1195–1198, 1984.

Murphree, J. S., S. Ismail, L. L. Cogger, D. D. Wallis, G. G. Shepherd, R. Link, and D. M. Klumpar, Characteristics of optical emissions and particle precipitation in polar cap arcs, *Planet. Space Sci.*, *31*, 161–172, 1983.

Rasmussen, C. E., R. W. Schunk, J. J. Sojka, V. B. Wickwar, O. de la Beaujardiere, J. Foster, J. Holt, D. S. Evans, and E. Nielsen, Comparison of simultaneous Chatanika and Millstone Hill observations with ionospheric model predictions, *J. Geophys. Res.*, *91*, 6986–6998, 1986.

Rees, M. H., Excitation of $O(^1S)$ and emission of 5577Å radiation in aurora, *Planet. Space Sci.*, *32*, 373–378, 1984.

Rees, M. H., and D. Luckey, Auroral electron energy derived from ratio of spectroscopic emissions, 1, Model computations, *J. Geophys. Res.*, *79*, 5181–5186, 1974.

Robinson, R. M., S. B. Mende, R. R. Vondrak, J. U. Kozyra, and A. F. Nagy, Radar and photometric measurements of an intense type A red aurora, *J. Geophys. Res.*, *90*, 457–466, 1985.

Robinson, R. M., R. R. Vondrak, K. Miller, T. Dabbs, and D. Hardy, On calculating ionospheric conductances from the flux and energy of precipitating electrons, *J. Geophys. Res.*, *92*, 2565–2569, 1987.

Roble, R. G., E. C. Ridley, and R. E. Dickenson, On the global mean structure of the thermosphere, *J. Geophys. Res.*, *92*, 8745–8758, 1987.

Schunk, R. W., and W. J. Raitt, Atomic nitrogen and oxygen ions in the daytime high-latitude F region, *J. Geophys. Res.*, *85*, 1255–1272, 1980.

Schunk, R. W., and J. J. Sojka, Ion temperature variations in the daytime high-latitude F region, *J. Geophys. Res.*, *87*, 5169–5183, 1982.

Schunk, R. W., and J. C. G. Walker, Theoretical ion densities in the lower ionosphere, *Planet. Space Sci.*, *21*, 1875–1896, 1973.

Schunk, R. W., W. J. Raitt, and P. M. Banks, Effect of electric fields on the daytime high-latitude E and F regions, *J. Geophys. Res.*, *80*, 3121–3130, 1975.

Schunk, R. W., P. M. Banks, and W. J. Raitt, Effects of electric fields and other processes upon the nighttime high latitude F layer, *J. Geophys. Res.*, *81*, 3271–3282, 1976.

Sharp, W. E., M. H. Rees, and A. I. Stewart, Coordinated rocket and satellite measurements of an auroral event, 2, The rocket observations and analysis, *J. Geophys. Res.*, *84*, 1977–1985, 1979.

Shepherd, G. G., J. D. Winningham, F. E. Bunn, and F. W. Thirkettle, An empirical determination of the production efficiency for auroral 6300-Å emission by energetic electrons, *J. Geophys. Res.*, *85*, 715–721, 1980.

Sojka, J. J., and R. W. Schunk, A theoretical study of the high latitude F region's response to magnetospheric storm inputs, *J. Geophys. Res.*, *88*, 2112–2122, 1983.

Sojka, J. J., and R. W. Schunk, A theoretical F region study of ion compositional and temperature variations in response to magnetospheric storm inputs, *J. Geophys. Res.*, *89*, 2348–2358, 1984.

Sojka, J. J., and R. W. Schunk, A theoretical study of the global F region for June solstice, solar maximum, and low magnetic activity, *J. Geophys. Res.*, *90*, 5285–5298, 1985.

Sojka, J. J., W. J. Raitt, and R. W. Schunk, A theoretical study of the high-latitude winter F region at solar minimum for low magnetic activity, *J. Geophys. Res.*, *86*, 609–621, 1981a.

Sojka, J. J., W. J. Raitt, and R. W. Schunk, Theoretical predictions for ion composition in the high-latitude winter F region for solar minimum and low magnetic activity, *J. Geophys. Res.*, *86*, 2206–2216, 1981b.

Sojka, J. J., W. J. Raitt, and R. W. Schunk, Plasma density features associated with strong convection in the winter high-latitude F region, J. Geophys. Res., 86, 6908–6916, 1981c.

Sojka, J. J., R. W. Schunk, J. V. Evans, J. M. Holt, and R. H. Wand, Comparison of model high-latitude electron densities with Millstone Hill observations, J. Geophys. Res., 88, 7783–7793, 1983.

Sojka, J. J., C. E. Rasmussen, and R. W. Schunk, An interplanetary magnetic field dependent model of the ionospheric convection electric field, J. Geophys. Res., 91, 11281–11290, 1986.

Spiro, R. W., P. H. Reiff, and L. J. Maher, Precipitating electron energy flux and auroral zone conductances: An empirical model, J. Geophys. Res., 87, 8215–8227, 1982.

Volland, H., A model of the magnetospheric electric convection field, J. Geophys. Res., 83, 2695–2699, 1978.

Winningham, J. D., T. W. Speiser, E. W. Hones, Jr., R. A. Jeffries, W. H. Roach, D. S. Evans, and H. C. Stenbaek-Nielsen, Rocket-borne measurements of the dayside cleft plasma: The Tordo experiments, J. Geophys. Res., 82, 1876–1888, 1977.

Winningham, J. D., J. L. Burch, N. Eaker, V. A. Blevins, and R. A. Hoffman, The low altitude plasma instrument (LAPI), Space Sci. Instrum., 5, 465–475, 1981.

World Data Center C2 for Geomagnetism, Data Book 10, Fac. of Sci., Kyota University, Kyoto, Japan, 1984.

J. D. Craven and L. A. Frank, Department of Physics and Astronomy, Univeristy of Iowa, Iowa City, IA 52242.

R. W. Schunk and J. J. Sojka, Center for Atmospheric and Space Sciences, Utah State University, Logan, UT 84322.

J. Sharber and J. D. Winningham, Southwest Research Insitute, P. O. Drawer 28510, San Antonio, TX 78284.